

Article

Sliding Mode Active Disturbance Rejection Control of Permanent Magnet Synchronous Motor Based on Improved Genetic Algorithm

Shuai Li ^{1,2,3}, Henian Li ^{1,2,3}, Hai Wang ^{1,2,3,*}, Chunlai Yang ^{1,2,3}, Jingsong Gui ⁴ and Ronghua Fu ⁵¹ School of Mechanical Engineering, Anhui Polytechnic University, Wuhu 241000, China² Anhui Key Laboratory of Advanced Numerical Control and Servo Technology, Wuhu 241000, China³ Anhui Polytechnic University Industrial Innovation Technology Research Co., Ltd., Wuhu 241000, China⁴ Wuhu Ruilong Robot Technology Co., Ltd., Wuhu 241000, China⁵ Wuhu Googol Automation Technology Co., Ltd., Wuhu 241000, China

* Correspondence: wanghai@ahpu.edu.cn

Abstract: Sliding mode control has been widely used to control permanent magnet synchronous motors (PMSM). However, the parameters of the sliding mode controller are difficult to be tuned, which makes the control performance of PMSM hard to be improved. A nonlinear sliding mode control method that integrated a nonlinear reaching law (NRLSMC) and extended state observer (ESO) is proposed in this paper, whose parameters are tuned by an improved genetic algorithm (IGA). The control performance of the nonlinear reaching law in the nonlinear sliding mode controller is analyzed, whose stability is verified based on the Lyapunov theorem. An extended state observer is integrated into the above controller to further improve the anti-interference capability, and compensate for the observed external disturbance of the system into the speed controller in sliding mode. The optimal parameters of the above sliding mode control are tuned by IGA combined with the system speed loop model. The performance of the proposed controller is numerically simulated in MATLAB/Simulink and verified in a control system rapid control prototype (RCP) experimental platform built based on dSPACE 1202. Numerical simulation and experimental results show that the proposed controller can make the PMSM control system with the advantages of no overshoot, fast response, and strong robustness.

Keywords: permanent magnet synchronous motor; sliding mode control; improved genetic algorithm; nonlinear reaching law; extended state observer; dSPACE 1202

Citation: Li, S.; Li, H.; Wang, H.; Yang, C.; Gui, J.; Fu, R. Sliding Mode Active Disturbance Rejection Control of Permanent Magnet Synchronous Motor Based on Improved Genetic Algorithm. *Actuators* **2023**, *12*, 209. <https://doi.org/10.3390/act12050209>

Academic Editor: Ioan Ursu

Received: 16 April 2023

Revised: 13 May 2023

Accepted: 18 May 2023

Published: 19 May 2023



Copyright: © 2023 by the authors. Licensee MDPI, Basel, Switzerland. This article is an open access article distributed under the terms and conditions of the Creative Commons Attribution (CC BY) license (<https://creativecommons.org/licenses/by/4.0/>).

1. Introduction

Permanent magnet synchronous motor (PMSM) is widely used in civil engineering, aerospace, and industry owing to its simple structure and excellent control performance. The control of PMSM usually used the traditional PID controlled with simple structure. However, the performance of PID control is highly relied on an accurate system model, which makes it easily affected by external disturbances or motor parameters perturbation. Several control algorithms are developed in recent years to improve the control performance of PMSM, such as adaptive control [1,2], optimal control [3], backstepping control [4], fuzzy control [5,6], sliding mode control (SMC) [7,8] and model predictive control [9]. Sliding mode control is widely used in PMSM, which does not involve precise mathematical models and is highly insensitive to external noise disturbances and motor parameters perturbations. However, the reaching laws used in traditional sliding mode control are equal reaching law, exponential reaching law, and power reaching law, which causes reaching rate of the controller too slow to converge in finite time, sometime generates

jitter. Additionally, the parameters of the traditional sliding mode control are tuned independently based on tuning methods such as the trial-and-error method and the empirical method, which leads to low tuning efficiency and large errors.

To solve the problems of slow reaching rate and jitter in the traditional sliding mode control, Y Li et al. [10] proposed an improved fast variable power reaching law by adding a variable exponential term to the original fast double power reaching law, which improves the reaching rate of the system and limits the jitter phenomenon with finite convergence time. C Chen et al. [11] introduced the variable containing the stator current estimation information as the gain of the isokinetic reaching term in the traditional exponential reaching law, so that the sliding mode observer adaptively adjusts the convergence rate with the change of the system state and improves the steady-state performance. E L Kang et al. [12] designed a non-singular fast terminal sliding mode surface by combining a non-linear function with a linear function to achieve a fast convergence of the system error at different stages. To further improve the anti-interference capability of the control system, L Z Qu et al. [13] estimated the total system disturbance with an extended state observer and compensated it to the sliding mode speed controller, which improved the speed tracking performance and anti-disturbance robustness of the controller under different disturbances such as internal parameter changes and external load changes, while maintaining a fast dynamic response. E Lu et al. [14] proposed a second-order non-singular terminal sliding mode observer that estimates the external load disturbances of the controller and improves the anti-interference capability of the system.

Several optimal algorithms are proposed by researchers in recent years to solve the difficulty of sliding mode parameters tuning. R Y Zhang et al. [15] used an improved particle swarm algorithm based on the Corsi variant to optimize the parameters of the PMSM vector control speed loop PI controller, which improved speed control accuracy significantly. J Z Yan et al. [16] performed online self-tuning and optimization of PID controller parameters by combining the reward of reinforcement learning, experience playback mechanism, and dynamic performance index evaluation module of the control system, which simplified the tuning process, reduced the overshoot of the controlled quantity and improved the dynamic response performance of the controller effectively compared to the traditional method. L Z Feng et al. [17] proposed an optimization algorithm for Drosophila based on a dual drive of multiple repellents and multiple lures. The PID controller with the above parameter tuning method has the advantages of small error, fast response time, and high stability, compared with other optimization algorithms. L Q Xiao [18] proposed a method based on an improved genetic algorithm to tune the PID controller parameters, which improves the convergence speed and accuracy compared to the ordinary genetic algorithm and can increase the probability of convergence to the optimal value. Tran H K et al. [19] proposed an improved genetic algorithm that speeds up convergence and saves operation time by ignoring the chromosome decoding step and uses the integral of squared error (ISE) as the fitness function for finding the optimal values of the fuzzy PID control parameters. However, the above tuning methods are mostly applied in PI or PID controller parameters, which are unsuitable for sliding mode control of PMSM.

A nonlinear reaching law sliding mode control (NRLSMC) is proposed in this paper, to solve the above problems in traditional sliding mode control, such as slow reaching rate and jitter. In addition, an extended state observer (ESO) is introduced in the proposed controller to further improve the anti-interference capability of the control system. The external disturbances observed by the ESO can be used to compensate for the NRLSMC speed controller. Meanwhile, an improved genetic algorithm (IGA) is used to tune the parameters of NRLSMC. The IGA can adaptively change with the fitness value compared to the normal GA [20,21], which can effectively reduce the probability of falling into a local optimal solution and increase the convergence speed. Finally, the performance of NRLSMC is numerically simulated in MATLAB/Simulink, and validated through experiments on a rapid control prototype (RCP) experimental platform based on dSPACE 1202 [22–24]. Both simulation and experimental results show that the controller can make the

PMSM control system with the advantages of no overshoot, fast response, and strong robustness.

2. Principle and Mathematical Model of PMSM

2.1. PMSM Principle

The schematic diagram of the principle of permanent magnet synchronous motor is shown in Figure 1. The three-phase symmetrical current is introduced into the three pairs of stator windings to generate a rotating magnetic field, which interacts with the permanent magnet on the rotor to drive the rotor to rotate.

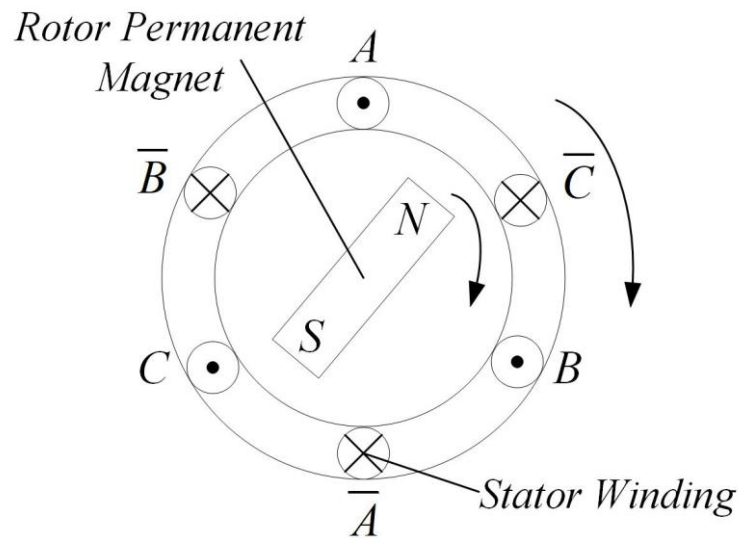


Figure 1. Schematic diagram of PMSM.

2.2. Mathematical Model of PMSM

According to the mathematical model of the hidden-pole permanent magnet synchronous motor ($L_d=L_q=L_s$) on the three-phase stationary coordinate system, after coordinating transformation, the mathematical model of the PMSM on the two-phase rotating coordinate system (d - q coordinate system) is obtained as follows.

1. Voltage equation

$$\begin{pmatrix} u_d \\ u_q \end{pmatrix} = \begin{pmatrix} R_s + pL_d & 0 \\ 0 & R_s + pL_q \end{pmatrix} \begin{pmatrix} i_d \\ i_q \end{pmatrix} + \begin{pmatrix} e_{rd} \\ e_{rq} \end{pmatrix} \quad (1)$$

$$\begin{pmatrix} e_{rd} \\ e_{rq} \end{pmatrix} = \begin{pmatrix} 0 & -\omega_e L_q \\ \omega_e L_d & 0 \end{pmatrix} \begin{pmatrix} i_d \\ i_q \end{pmatrix} + \begin{pmatrix} 0 \\ \psi_f \end{pmatrix} \quad (2)$$

where R_s is the stator resistance; L_d and L_q are the components of the stator winding self-inductance on the d - q axis; $p = d/dt$ is the differential operator; e_{rd} and e_{rq} are the rotating electric potentials on the d - q axis; ω_e is the electric angular velocity; ψ_f is the permanent magnet magnetic chain.

2. Torque equation

$$T_e = \frac{3}{2} n_p \left[(L_d i_d + \psi_f) i_q - (L_q i_q) i_d \right] \quad (3)$$

where n_p is the number of magnetic pole pairs.

3. Motion equation

(4)

where T_L is the load torque; J is the rotational inertia; ω_m is the mechanical angular velocity; and B is the damping factor.

3. Design of Sliding Mode Speed Controller

3.1. Nonlinear Reaching Law

The reaching law is the key factor that affects the performance of the sliding mode speed controller. Appropriate reaching law can increase the reach rate to the sliding mode surface and suppress the jitter problem inherent in the sliding mode effectively.

The three types of traditional reaching laws used in sliding mode control are listed below:

1. Power reaching law:

$$\dot{s} = -k |s|^\alpha \operatorname{sgn}(s) \quad k > 0, 1 > \alpha > 0 \quad (5)$$

2. Exponential reaching law:

$$\dot{s} = -\varepsilon \operatorname{sgn}(s) - ks \quad \varepsilon, k > 0 \quad (6)$$

3. Rapid power reaching law:

$$\dot{s} = -\varepsilon |s|^\alpha \operatorname{sgn}(s) - ks \quad \varepsilon, k > 0, 1 > \alpha > 0 \quad (7)$$

The traditional reaching laws cannot realize rapid reaching rate and jitter weakening simultaneously, which results in poor controller control performance. To solve the above problems in the sliding mode controller, a nonlinear reaching law is designed as below:

$$\dot{s} = -\varepsilon \tanh(|x_1|) |s|^\alpha \operatorname{sgn}(s) - ke^{\beta|x_1|} s \quad (8)$$

where s is the sliding mode surface; x_1 is the state variable, $\lim_{s \rightarrow 0} |x_1| = 0$; $\varepsilon > 0$, $0 < \alpha < 1$, $k > 0$, $\beta > 0$.

From Equation (8), it can be seen that when the system is far from the sliding surface, s is larger, where $ke^{\beta|x_1|} s$ plays a major role, and due to the adding of the exponential term $e^{\beta|x_1|}$, the reaching rate is effectively enhanced, which can make the system reaching the sliding mode surface faster. When the system is close to the sliding mode surface, s is smaller, where $-\varepsilon \tanh(|x_1|) |s|^\alpha \operatorname{sgn}(s)$ plays a major role, and $\lim_{s \rightarrow 0} |x_1| = 0$, $\tanh(|x_1|)$ tends to 0, and $\varepsilon \tanh(|x_1|) |s|^\alpha \operatorname{sgn}(s)$ tends to 0 faster than the power reaching law, which effectively weakens the jitter. Meanwhile, the coefficient β is introduced to adjust the reaching rate of the system when s changes to fit various systems; the state variable x_1 is introduced to suppress the jitter generated by the exponential term.

3.2. Performance of Nonlinear Reaching Law

Taking the linear system shown in Equation (9) as an example, the control performance is analyzed for the power-reaching law, exponential reaching law, rapid power-reaching law, and the nonlinear reaching law designed in this paper, respectively.

$$\dot{\mathbf{x}} = \mathbf{A}\mathbf{x} + \mathbf{B}\mathbf{u} \quad (9)$$

Define the sliding mode surface function:

$$\mathbf{s} = \mathbf{C}\mathbf{x} \quad (10)$$

Derivative of Equation (10):

$$\dot{\mathbf{s}} = \mathbf{C}\dot{\mathbf{x}} \quad (11)$$

According to Equations (8), (9), and (11), the nonlinear reaching law controller function is obtained as follows:

$$\mathbf{u} = (\mathbf{CB})^{-1}[-\mathbf{CA}\mathbf{x} - \varepsilon \tanh(|x_1|)|\mathbf{s}|^\alpha \operatorname{sgn}(\mathbf{s}) - ke^{\beta|x_1|}\mathbf{s}] \quad (12)$$

where $\mathbf{x} = \begin{pmatrix} x_1 \\ x_2 \end{pmatrix}$, x_1, x_2 is the control system state variable; u is the control system control variable; $\mathbf{A}, \mathbf{B}, \mathbf{C}$ is the control system constant matrix.

The four reaching laws control system constant matrices involved in the comparison are all defined as $\mathbf{A} = \begin{pmatrix} 0 & 1 \\ 0 & -25 \end{pmatrix}$, $\mathbf{B} = \begin{pmatrix} 0 \\ 133 \end{pmatrix}$, $\mathbf{C} = (20 \ 1)$ [25,26]; the initial state variables of the control system are all defined as $\mathbf{x} = \begin{pmatrix} 5 \\ 5 \end{pmatrix}$; the four reaching laws coefficients are shown in Table 1.

Table 1. Reaching law coefficients.

Reaching Law	Coefficient
Power reaching law	$k = 30, \alpha = 0.5$
Exponential reaching law	$\varepsilon = 5, k = 30$
Rapid power reaching law	$\varepsilon = 5, \alpha = 0.5, k = 30$
Nonlinear reaching law	$\varepsilon = 5, \alpha = 0.5, k = 30, \beta = 0.7$

The simulation results of the control performance of the four reaching laws are shown in Figure 1.

As shown in Figure 2a, the nonlinear reaching law can make the system reach the sliding mode surface faster than the other three reaching laws. As shown in Figure 2b, the controller output of the nonlinear reaching law reaches a steady state fastest without jitter, compared to other reaching laws. The convergence process of the sliding mode surface function s and state variables x_1, x_2 are shown in Figure 2c–e. It can be seen that the nonlinear reaching law sliding mode surface function and state variables have the fastest convergence speed compared with the other three reaching laws. Therefore, the nonlinear reaching law designed in this paper can effectively improve the reaching rate and weaken the sliding mode jitter simultaneously.

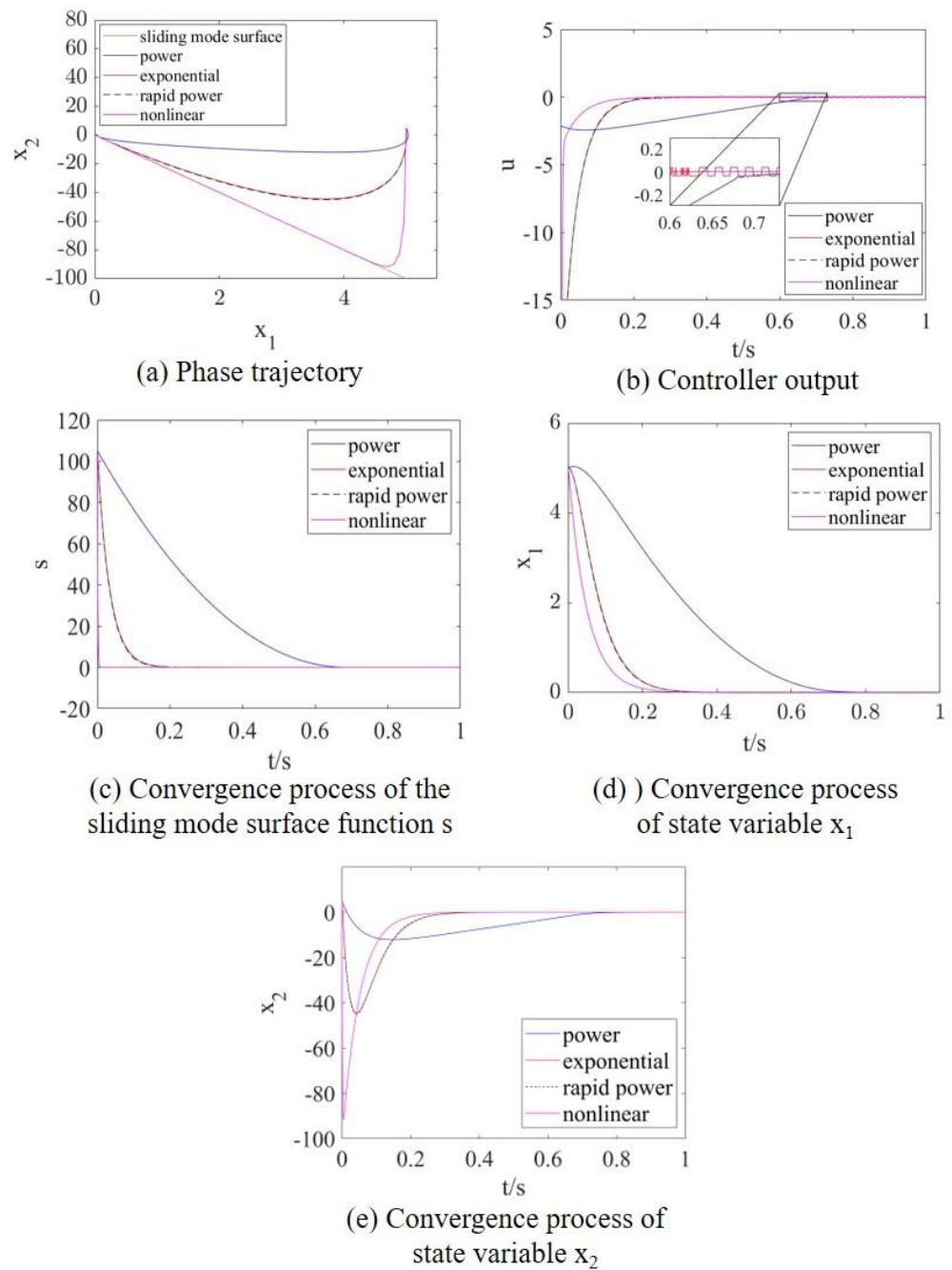


Figure 2. Simulation results of the control performance of the four reaching laws.

3.3. Sliding Mode Speed Controller Design Based on Nonlinear Reaching Law

According to Equations (1), (3), and (4), and $\omega_e = n_p \omega_m$, when the control method with $i_a = 0$ is used, we can get:

$$\frac{di_q}{dt} = \frac{1}{L_q} (u_q - R_s i_q - n_p \omega_m \psi_f) \quad (13)$$

$$\frac{d\omega_m}{dt} = \frac{1}{J} \left(\frac{3}{2} n_p \psi_f i_q - T_L - B \omega_m \right) \quad (14)$$

Define the state and control variables of the PMSM control system:

$$\begin{cases} x_1 = \omega_{ref} - \omega_m \\ x_2 = \dot{x}_1 = -\dot{\omega}_m \\ u = \dot{i}_q \end{cases} \quad (15)$$

where ω_{ref} is the reference angular speed of the motor.

According to Equations (14) and (15), we can get:

$$\begin{cases} \dot{x}_1 = x_2 \\ \dot{x}_2 = -\frac{3}{2J}n_p\psi_f u - \frac{B}{J}x_2 \end{cases} \quad (16)$$

Let $D = \frac{3}{2J}n_p\psi_f$, then the state equation of the control system is:

$$\begin{pmatrix} \dot{x}_1 \\ \dot{x}_2 \end{pmatrix} = \begin{pmatrix} 0 & 1 \\ 0 & -\frac{B}{J} \end{pmatrix} \begin{pmatrix} x_1 \\ x_2 \end{pmatrix} + \begin{pmatrix} 0 \\ -D \end{pmatrix} u \quad (17)$$

Define the sliding mode surface function:

$$s = cx_1 + x_2 \quad (18)$$

Derivative of Equation (18):

$$\dot{s} = (c - \frac{B}{J})x_2 - Du \quad (19)$$

The output of the sliding mode speed controller with nonlinear reaching law can be obtained according to Equations (8), (15), and (19), such as:

$$i_q^* = \int u dt = \frac{1}{D} \int [(c - \frac{B}{J})x_2 + \varepsilon \tanh(|x_1|)|s|^\alpha \operatorname{sgn}(s) + ke^{\beta|x_1|}s] dt \quad (20)$$

where i_q^* is the q -axis reference current; $c > 0$, $\varepsilon > 0$, $0 < \alpha < 1$, $k > 0$, $\beta > 0$.

3.4. Proof of Stability

Theorem 1. For the state and control variables of the PMSM control system shown in Equation (15), selecting the sliding mode surface shown in Equation (18), and selecting the nonlinear reaching law shown in Equation (8), the designed sliding mode speed controller Equation (20) is asymptotically stable.

Proof. Select the Lyapunov function:

$$V = \frac{1}{2}s^2 \quad (21)$$

Derivative of Equation (21):

$$\dot{V} = s\dot{s} \quad (22)$$

Substituting Equation (8) into Equation (22), we can get:

$$\lim_{s \rightarrow 0} \dot{V} = \lim_{s \rightarrow 0} [s(-\varepsilon \tanh(|x_1|)|s|^\alpha \operatorname{sgn}(s) - ke^{\beta|x_1|}s)] \leq 0 \quad (23)$$

when and only when $s = 0$, $\dot{V} = s\dot{s} = 0$.

Therefore, the designed nonlinear reaching law satisfies the sliding mode reachability condition, that is, the sliding mode speed controller is asymptotically stable. \square

Discretization of nonlinear reaching law sliding mode speed controller.

To transform the continuity problem into the discrete problem that the computer can handle in the rapid control prototype experiment, the nonlinear reaching law sliding mode speed controller needs to be discretized.

Consider the following discrete linear system free of uncertainties and perturbations:

$$\mathbf{x}(k+1) = \mathbf{A}\mathbf{x}(k) + \mathbf{b}\mathbf{u}(k) \quad (24)$$

$$\text{where } \mathbf{x}(k) = \begin{pmatrix} x_1(k) \\ x_2(k) \end{pmatrix}.$$

According to Equation (17), we can know the equation of state of the control system as:

$$\dot{\mathbf{x}} = \mathbf{A}_1\mathbf{x} + \mathbf{b}_1\mathbf{u} \quad (25)$$

$$\text{where } \mathbf{A}_1 = \begin{pmatrix} 0 & 1 \\ 0 & -\frac{B}{J} \end{pmatrix}, \mathbf{b}_1 = \begin{pmatrix} 0 \\ -D \end{pmatrix}, \mathbf{x} = \begin{pmatrix} x_1 \\ x_2 \end{pmatrix}.$$

The first order Euler discretization of Equation (25) gives:

$$\frac{\mathbf{x}(k+1) - \mathbf{x}(k)}{T} = \mathbf{A}_1\mathbf{x}(k) + \mathbf{b}_1\mathbf{u}(k) \quad (26)$$

where T is the sample period.

From equation (26), we can obtain:

$$\mathbf{x}(k+1) = (T\mathbf{A}_1 + \mathbf{E})\mathbf{x}(k) + T\mathbf{b}_1\mathbf{u}(k) \quad (27)$$

Then, according to Equation (24) we can get: $\mathbf{A} = T\mathbf{A}_1 + \mathbf{E}$, $\mathbf{b} = T\mathbf{b}_1$.

Define the discrete sliding mode surface function:

$$\mathbf{s}(k) = \mathbf{C}^T \mathbf{x}(k) \quad (28)$$

where $\mathbf{C}^T = (c \ 1)$.

According to Equations (24) and (28), we can obtain:

$$\mathbf{s}(k+1) - \mathbf{s}(k) = (\mathbf{C}^T \mathbf{A} - \mathbf{C}^T) \mathbf{x}(k) + \mathbf{C}^T \mathbf{b}\mathbf{u}(k) \quad (29)$$

The nonlinear reaching law can be discretized as follows:

$$\frac{\mathbf{s}(k+1) - \mathbf{s}(k)}{T} = -\varepsilon \tanh(|x_1(k)|) |\mathbf{s}(k)|^\alpha \text{sgn}(\mathbf{s}(k)) - k e^{\beta|x_1(k)|} \mathbf{s}(k) \quad (30)$$

According to Equations (29) and (30), we can obtain:

$$-\varepsilon T \tanh(|x_1(k)|) |\mathbf{s}(k)|^\alpha \text{sgn}(\mathbf{s}(k)) - k T e^{\beta|x_1(k)|} \mathbf{s}(k) = (\mathbf{C}^T \mathbf{A} - \mathbf{C}^T) \mathbf{x}(k) + \mathbf{C}^T \mathbf{b}\mathbf{u}(k) \quad (31)$$

From Equation (31), the discretized nonlinear reaching law sliding mode speed controller function is obtained as:

$$\mathbf{u}(k) = (\mathbf{C}^T \mathbf{b})^{-1} \left[-\varepsilon T \tanh(|x_1(k)|) |\mathbf{s}(k)|^\alpha \text{sgn}(\mathbf{s}(k)) - k T e^{\beta|x_1(k)|} \mathbf{s}(k) - (\mathbf{C}^T \mathbf{A} - \mathbf{C}^T) \mathbf{x}(k) \right] \quad (32)$$

$$\text{where } \begin{cases} x_1(k) = \omega_{ref}(k) - \omega_m(k) \\ x_2(k) = \frac{x_1(k+1) - x_1(k)}{T} \\ \mathbf{C}^T \mathbf{b} = -TD \\ \mathbf{C}^T \mathbf{A} - \mathbf{C}^T = \begin{pmatrix} 0 & \left(c - \frac{B}{J}\right)T \end{pmatrix} \end{cases}$$

Then, the output of the discretized nonlinear reaching law sliding mode speed controller is:

$$\mathbf{i}_q^*(k) = T \sum \mathbf{u}(k) \quad (33)$$

4. Extended State Observer and Its Stability Proof

ESO is introduced in the NRLSMC speed controller to further improve the anti-interference capability of the control system. The ESO can observe the external disturbances of the system, and the observed total disturbances are used to compensate for the nonlinear reaching law sliding mode speed controller.

Considering the total disturbance $d(t)$ from parameter uncertainty, load torque, external disturbance torque and q -axis current tracking error suffered by the speed loop, Equation (14) can be rewritten as:

$$\frac{d\omega_m(t)}{dt} = Di_q(t) - \frac{B}{J}\omega_m(t) + d(t) \quad (34)$$

The following state variables are defined:

$$\begin{cases} x_1(t) = \omega_m(t) \\ x_2(t) = d(t) \end{cases} \quad (35)$$

According to Equations (34) and (35), the extended state system is obtained as follows:

$$\begin{cases} \dot{x}_1(t) = Di_q(t) - \frac{B}{J}x_1(t) + x_2(t) \\ \dot{x}_2(t) = \Delta(t) \end{cases} \quad (36)$$

where $\Delta(t)$ is the rate of change of $d(t)$.

The linear ESO of the system can be designed according to Equation (36):

$$\begin{cases} e_1(t) = z_1(t) - x_1(t) \\ e_2(t) = z_2(t) - x_2(t) \\ \dot{z}_1(t) = Di_q(t) - \frac{B}{J}z_1(t) + z_2(t) - 2\gamma e_1(t) \\ \dot{z}_2(t) = -\gamma^2 e_1(t) \end{cases} \quad (37)$$

where γ is the ESO parameter to be designed, $\gamma > 0$; $e_1(t)$ is the ω_m observation error; $e_2(t)$ is the $d(t)$ observation error; $z_1(t)$ is the ω_m observation value; $z_2(t)$ is the $d(t)$ observation value.

The total disturbance $z_2(t)$ observed in Equation (37) is compensated into the designed nonlinear reaching law sliding mode speed controller, and according to Equation (20), the output of the nonlinear reaching law sliding mode speed controller is:

$$i_q^* = \frac{1}{D} \int [(c - \frac{B}{J})x_2 + \varepsilon \tanh(|x_1|)|s|^\alpha \operatorname{sgn}(s) + ke^{\beta|x_1|}s] dt - \frac{z_2(t)}{D} \quad (38)$$

The parameter γ of the ESO to be designed determines the bandwidth of the ESO, but the too-large value of γ can increase the observation noise. Therefore, the value of γ should be balanced between bandwidth and noise.

Defining the expanded state system:

$$\begin{cases} \dot{x}_1 = Di_q - \frac{B}{J}x_1 + x_2 \\ \dot{x}_2 = \Delta \quad y = x_1 \end{cases} \quad (39)$$

Rewrite Equation (39) as a system of state matrix equations and let $i_q = u$.

$$\begin{cases} \dot{\mathbf{x}} = \mathbf{A} \cdot \mathbf{x} + \mathbf{B} \cdot \mathbf{u} + \mathbf{E} \cdot \Delta \\ \mathbf{y} = \mathbf{C} \cdot \mathbf{x} \end{cases} \quad (40)$$

$$\text{where } \mathbf{A} = \begin{bmatrix} -\frac{B}{J} & 1 \\ 0 & 0 \end{bmatrix}, \mathbf{B} = [D \quad 0]^T, \mathbf{E} = [0 \quad 1]^T, \mathbf{C} = [1 \quad 0].$$

Construct the full-dimensional state observer of the system as follows:

$$\begin{cases} \dot{\mathbf{Z}} = \mathbf{A} \cdot \mathbf{Z} + \mathbf{B} \cdot \mathbf{u} + \mathbf{L}(\mathbf{y} - \mathbf{y}) \\ \mathbf{y} = \mathbf{C} \cdot \mathbf{Z} \end{cases} \quad (41)$$

where $\mathbf{L} = [2\gamma, \gamma^2]^T$ is the gain matrix.

Denote the ESO estimation error as $\mathbf{e}_i = \mathbf{Z}_i - \mathbf{x}_i (i = 1, 2)$. The error state matrix equation is obtained by subtracting Equation (40) from Equation (41):

$$\dot{\mathbf{e}} = (\mathbf{A} - \mathbf{LC}) \cdot \mathbf{e} + \mathbf{E} \cdot \Delta \quad (42)$$

$$\text{where } \mathbf{A} - \mathbf{LC} = \begin{bmatrix} -\frac{B}{J} & 1 \\ -\gamma^2 & 0 \end{bmatrix}, \text{ then the characteristic polynomial of the error state matrix}$$

equation is:

$$\begin{aligned} \lambda(s) &= \det[s \cdot \mathbf{I} - (\mathbf{A} - \mathbf{LC})] \\ &= \begin{vmatrix} s + \frac{B}{J} + 2\gamma & -1 \\ \gamma^2 & s \end{vmatrix} \\ &= s^2 + (2\gamma + \frac{B}{J})s + \gamma^2 \end{aligned} \quad (43)$$

It is known that $\gamma > 0$, $\frac{B}{J} > 0$, then $2\gamma + \frac{B}{J} > 0$, $\gamma^2 > 0$. When Δ is bounded and the ESO is known to be stable according to the Routh Criterion [27].

5. Parameter Tuning of Sliding Mode Speed Controller

5.1. Design of IGA

To obtain satisfactory dynamic characteristics of the transition process, the absolute value of the error time integration performance index is used as the minimum target function J for parameter selection, and the squared term of the controller input is added to the function to prevent excessive control, and to avoid overshoot: if the system produces overshoot, the amount of overshoot is used as one of the optimal indexes.

$$\begin{cases} J = \int_0^{\infty} [\omega_1 |e(t)| + \omega_2 u^2(t)] dt + \omega_3 t_u & e(y(t)) \geq 0 \\ J = \int_0^{\infty} [\omega_1 |e(t)| + \omega_2 u^2(t) + \omega_4 |e(y(t))|] dt + \omega_3 t_u & e(y(t)) < 0 \end{cases} \quad (44)$$

where $e(t)$ is the system error; $e(y(t)) = y(t) - y(t - 1)$ is the system output error, $y(t)$ is the system output; $u(t)$ is the control input; t_u is the rise time; $\omega_1, \omega_2, \omega_3, \omega_4$ are weights, $\omega_4 \gg \max(\omega_1, \omega_2, \omega_3)$; the fitness function $f = 1/J$.

The parameters of the NRLSMC speed controller such as $c, \varepsilon, \alpha, k, \beta$ are tuned by the improved genetic algorithm proposed in this paper. Normal genetic algorithm is able to perform global optimization because it relies on crossover and mutation to continuously generate new individuals while selecting newly generated offspring and parental individuals for survival. However, its crossover and mutation probabilities are preset constant values. When the set crossover probability is too large, too many individuals in each generation will change, which is not conducive to search. When the set mutation probability is too small, it is not easy to generate new individuals, thus making the genetic algorithm blind and irregular. According to the characteristics of crossover and mutation probabilities, a new adaptive improved genetic algorithm is designed in this paper, and the crossover and mutation probabilities of this improved genetic algorithm can change adaptively with the fitness value, and its crossover probability P_c and mutation probability P_m are:

$$P_c = \begin{cases} P_{c1} - \frac{(P_{c1} - P_{c2})(f' - f_{avg})}{f_{max} - f_{avg}} & f' \geq f_{avg} \\ P_{c2} + \frac{(P_{c1} - P_{c2})(f_{avg} - f')}{f_{avg} - f_{min}} & f' < f_{avg} \end{cases} \quad (45)$$

$$P_m = \begin{cases} P_{m1} - \frac{(P_{m1} - P_{m2})(f_{max} - f)}{f_{max} - f_{avg}} & f \geq f_{avg} \\ P_{m2} + \frac{(P_{m1} - P_{m2})(f_{avg} - f)}{f_{avg} - f_{min}} & f < f_{avg} \end{cases} \quad (46)$$

where $P_{c1} = 0.9, P_{c2} = 0.6, P_{m1} = 0.1, P_{m2} = 0.001$; f' is the fitness of the individual with larger fitness in the crossover operation; f is the fitness of the individual in the mutation operation; f_{max} and f_{min} are the maximum and minimum fitness in each generation of individuals; f_{avg} is the average fitness of each generation of individuals.

According to Equations (45) and (46), it is known that individuals with higher fitness in each iteration will be given lower P_c and P_m values, which is beneficial to the preservation of good individuals; individuals with lower fitness will be given higher P_c and P_m values, which is a benefit to the change of inferior individuals and improves the convergence speed of the algorithm. Because the fitness of individuals involved in crossover and mutation operations is random, the crossover and mutation probabilities of individuals are also random according to Equations (45) and (46), which improves the randomness of

the algorithm and effectively solves the situation that ordinary genetic algorithms are easy to fall into local optimal solutions.

The flowchart of the improved genetic algorithm is depicted in Figure 3. This algorithm involves designing a fitness function, determining the initial population size, calculating the target function value for each individual, and iterating through selection, crossing, and mutation operations. The algorithm halts when the number of iterations surpasses a pre-defined threshold and outputs the minimum value of the target function from the final iteration.

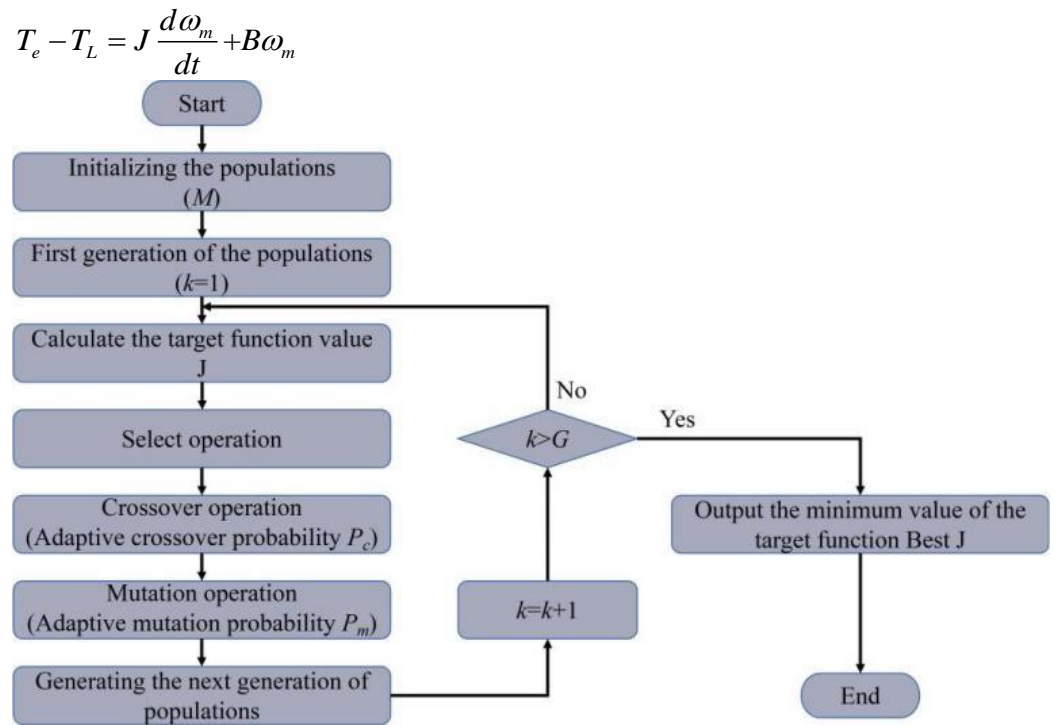


Figure 3. Flowchart of the improved genetic algorithm.

The improved genetic algorithm has the following three operational parameters that need to be set in advance:

1. M: number of individuals in the initialized population;
2. E: number of individual elements (number of parameters to be optimized);
3. G: number of iterations.

5.2. Modeling of Speed Loop

The parameter tuning method is an improved genetic algorithm combined with the PMSM nonlinear reaching law sliding mode control system speed loop MATLAB/Simulink simulation model. Hence, the speed loop simulation model of the system needs to be established as below.

Figure 4 shows the speed loop of the PMSM nonlinear reaching law sliding mode control system. As shown in Figure 4, to establish the system speed loop simulation model, we need to derive the system q -axis current loop closed-loop transfer function $G_i(s)_{close}$ first. The q -axis current loop adopts the PI controller, and the closed-loop transfer function is:

$$G_i(s)_{close} = \frac{G_i(s)_{open}}{1 + G_i(s)_{open}} \quad (47)$$

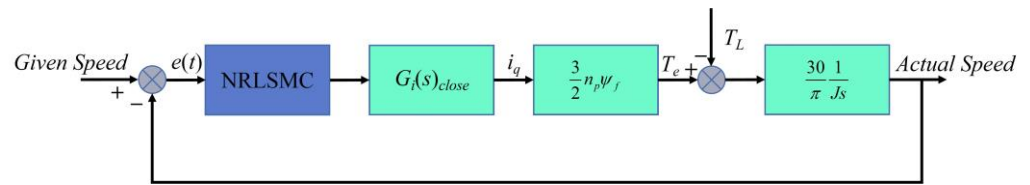


Figure 4. The speed loop of the PMSM nonlinear reaching law sliding mode control system.

The q -axis current loop consists of PI controller, PWM inverter and motor armature circuit, let the parameter $K_p = \tau_i K_i$ in PI controller, the current loop open loop transfer function can be obtained as follows:

$$G_i(s)_{open} = \frac{K_p (\tau_i s + 1)}{\tau_i s} \frac{K_{PWM}}{T_s s + 1} \frac{1}{L_q s + R_s} \tag{48}$$

where K_{PWM} is the PWM inverter gain and T_s is the PWM wave period.

Letting $\tau_i = L_q/R_s$ and $K_{PWM} = 1$, Equation (48) can be transformed into:

$$G_i(s)_{open} = \frac{K_p}{L_q s (T_s s + 1)} \tag{49}$$

According to Equations (47) and (49), the current loop closed-loop transfer function can be obtained as:

$$G_i(s)_{close} = \frac{1}{\frac{L_q}{K_p} T_s s^2 + \frac{L_q}{K_p} s + 1} = \frac{\frac{K_p}{L_q T_s}}{s^2 + \frac{1}{T_s} s + \frac{K_p}{L_q T_s}} \tag{50}$$

From the general form of the transfer function of the second-order system, we can get:

$$\begin{cases} \omega_n^2 = \frac{K_p}{L_q T_s} \\ 2\zeta\omega_n = \frac{1}{T_s} \\ \frac{L_q}{K_p} = 4\zeta^2 T_s \end{cases} \tag{51}$$

The q -axis current loop including in the speed loop can be considered as a first-order link, which can be obtained from Equations (50) and (51):

$$G_i(s)_{close} = \frac{1}{\frac{L_q}{K_p} s + 1} = \frac{1}{4\zeta^2 T_s s + 1} \tag{52}$$

Since the second-order system performs best at the damping ratio $\zeta = 0.707$, and the PWM wave period is set to $T_s = 1/15,000$ s, the current loop closed-loop transfer function is:

$$G_i(s)_{close} = \frac{7500}{s + 7500} \tag{53}$$

According to the actual motor parameters chosen $n_p = 4$, $\psi_f = 0.0084$ Wb, $J = 0.000028$ kg·m², we can get:

$$\begin{cases} \frac{3}{2} n_p \psi_f = 0.0504 \\ \frac{30}{\pi} \frac{1}{J s} = \frac{30}{0.000028 \pi s} \end{cases} \quad (54)$$

As shown in Figure 5, the speed loop of the PMSM nonlinear reaching law sliding mode control system MATLAB/Simulink simulation model can be constructed:

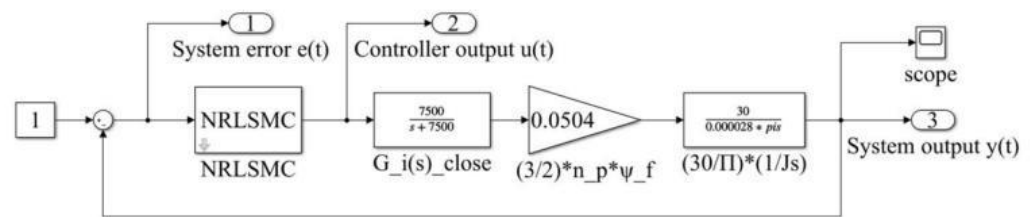


Figure 5. PMSM speed loop Simulink simulation model.

5.3. Parameter Tuning

Figure 6 shows the schematic diagram of the IGA combined with the Simulink simulation model. In the IGA, M groups of c , ε , α , k , and β are generated randomly in a specified range, which is tuned and stored in the workspace. Then, the Simulink model calls the M groups of parameters in the workspace and runs the model by sim function. The system error $e(t)$, control input $u(t)$, and system output $y(t)$ obtained after running are stored in the Workspace, and the IGA calls $e(t)$, $u(t)$ and $y(t)$ in the Workspace to calculate the M groups of target function values J. The above process is iterated until the best J is obtained.

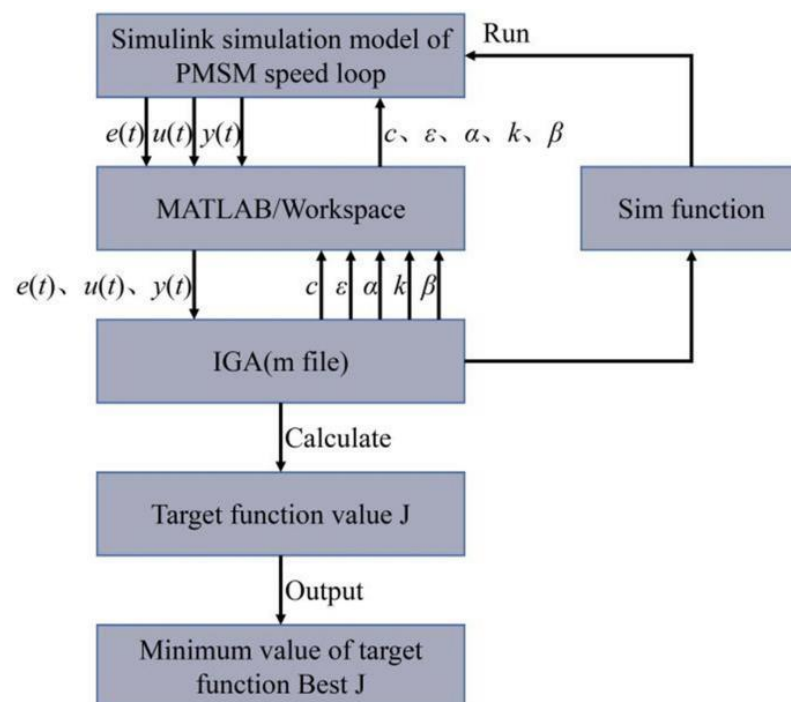


Figure 6. Schematic diagram of the IGA combined with Simulink simulation model.

Set the operating parameters of IGA: $M = 50$, $E = 5$, $G = 150$; the weights of the fitness function: $\omega_1 = 0.999$, $\omega_2 = 0.001$, $\omega_3 = 2.000$, and $\omega_4 = 100$; the setting of the range of values of the parameters to be tuned directly affects the iteration speed and global search ability of the algorithm, too large range will cause the algorithm iteration speed to be too slow, too small a range will cause the algorithm to fall into local optimal solutions. After repeated debugging, a group of satisfactory ranges of values for the parameters to be tuned are derived: $c \in (100, 300)$, $\varepsilon \in (0, 30)$, $\alpha \in (0, 1)$, $k \in (0, 150)$, and $\beta \in (0, 0.01)$.

Figure 7 shows the comparison of GA and IGA under the same operating parameters, in which, the crossover and mutation probabilities of the normal GA are set as $P_c = 0.9$ and $P_m = 0.1$, respectively. As shown in Figure 7a, the convergence speed of the best J of IGA is faster than GA. The best J converges at 101.8056 after 53 generations with IGA, while at 108.0853 after 114 generations with GA, which means the possibility of falling into the local optimal solutions is avoided effectively in IGA. As shown in Figure 7b, the response time of system output $y(t)$ in IGA is short than in GA. As shown in Figure 7c,d, the convergence speed of system error $e(t)$ and control input $u(t)$ in IGA is faster than GA. Therefore, the IGA has a faster convergence speed and better global search capability compared with GA. When the number of iterations reaches 150, the optimal values of the parameters of the nonlinear reaching law sliding mode speed controller corresponding to the minimum value of the target function output by the improved genetic algorithm are $c = 296.1473$, $\varepsilon = 29.3112$, $\alpha = 0.9678$, $k = 144.1718$, and $\beta = 0.0095$.

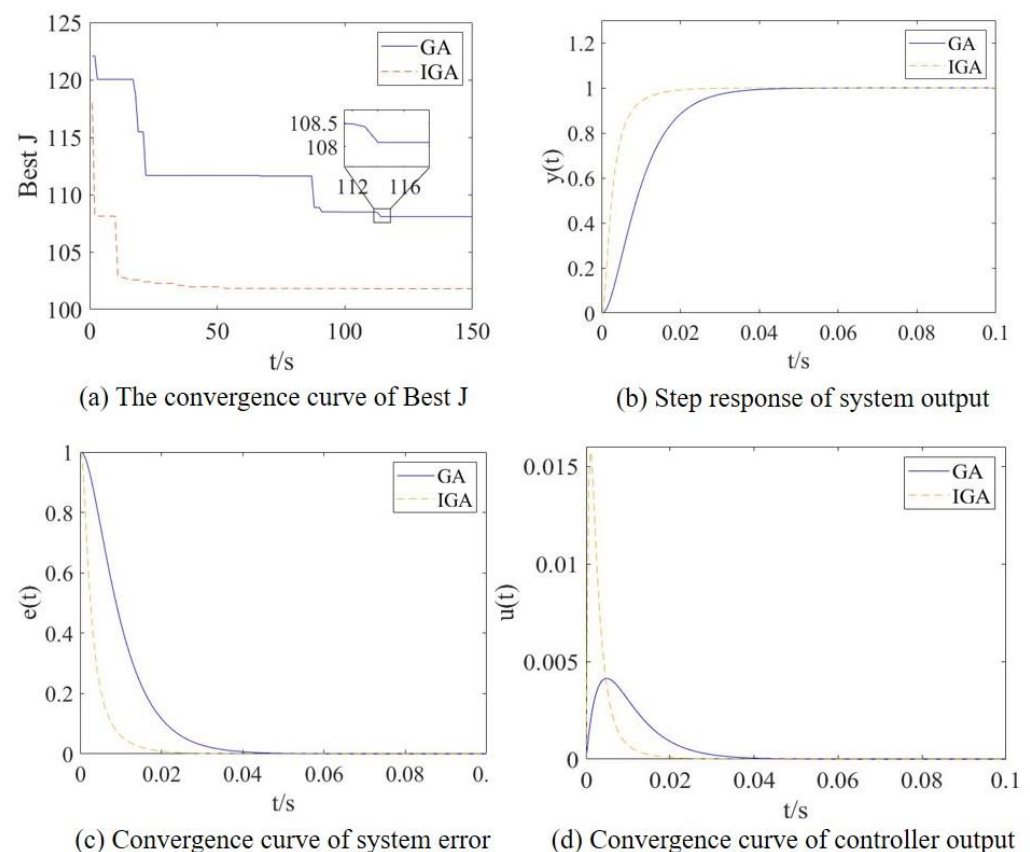


Figure 7. Comparison of GA and IGA.

Table 3. Speed controller parameters.

Speed Controller	Value
PID	$K_p=0.03, K_i=0.7, K_d=0.00005$
SMC	$c = 70, \varepsilon = 30, k = 500$
NRLSMC+ESO	$c = 230, \varepsilon = 30, \alpha = 0.5, k = 120, \beta = 0.005, \gamma = 4000$
IGA-NRLSMC+ESO	$c = 296.1473, \varepsilon = 29.3112, \alpha = 0.9678, k = 144.1718, \beta = 0.0095, \gamma = 4000$

Table 4. Current loop PI controller parameters.

Current Loop PI Controller	Value
<i>d</i> -axis current loop	$K_p=0.9, K_i=40$
<i>q</i> -axis current loop	$K_p=8.8, K_i=10$

Simulation conditions are set: bus voltage $U_{dc} = 24$ V, PWM switching frequency $f = 15$ kHz, sample period $T_s = 1 \times 10^{-6}$ s, ode23tb solver is used, the relative error is set to 1×10^{-6} , simulation time is set to 1 s, given speed $N_{ref} = 1000$ rpm, the motor is started at no load, 0.2 N·m load is applied at 0.5 s, and speed increases to 1200 rpm at 0.8 s. The simulation results are shown in Figures 9–15.

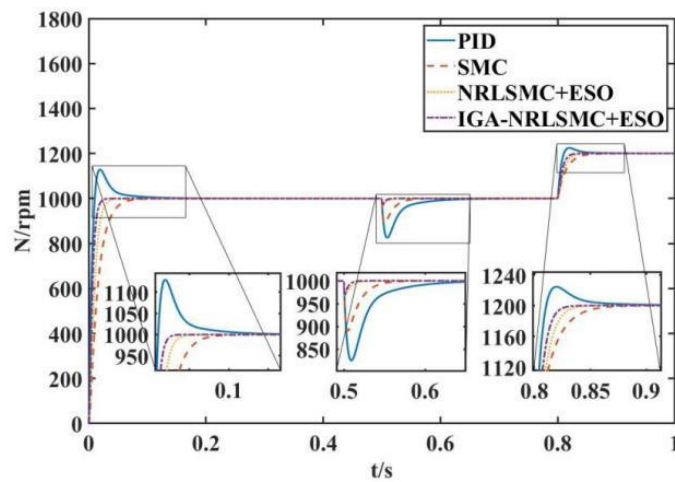


Figure 9. Speed curve.

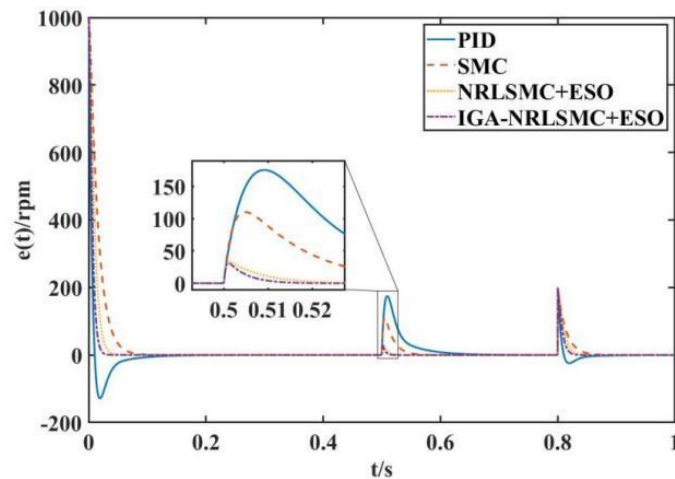


Figure 10. Speed error curve.

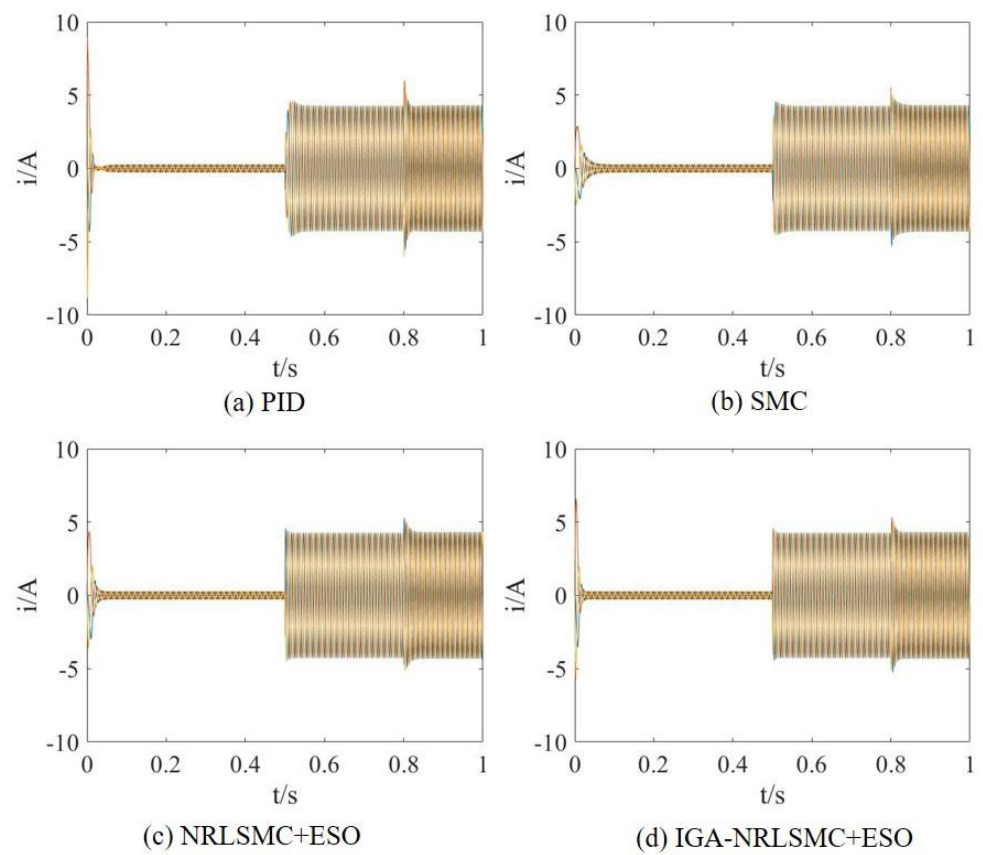


Figure 11. Three-phase current curve.

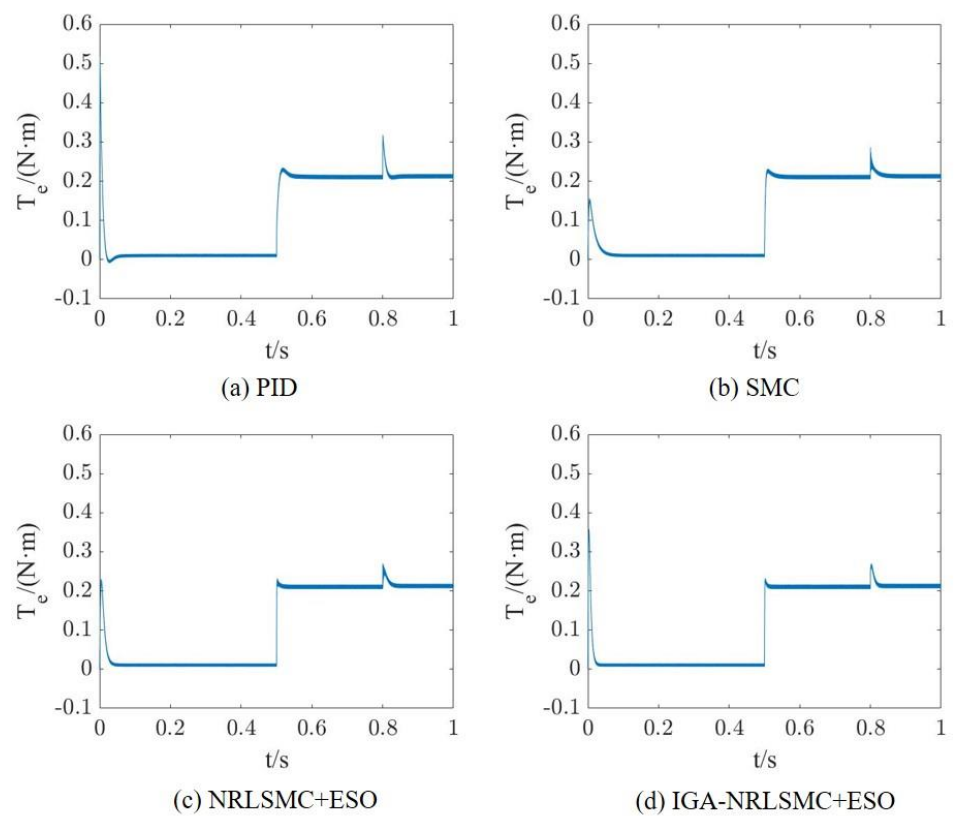


Figure 12. Torque curve.

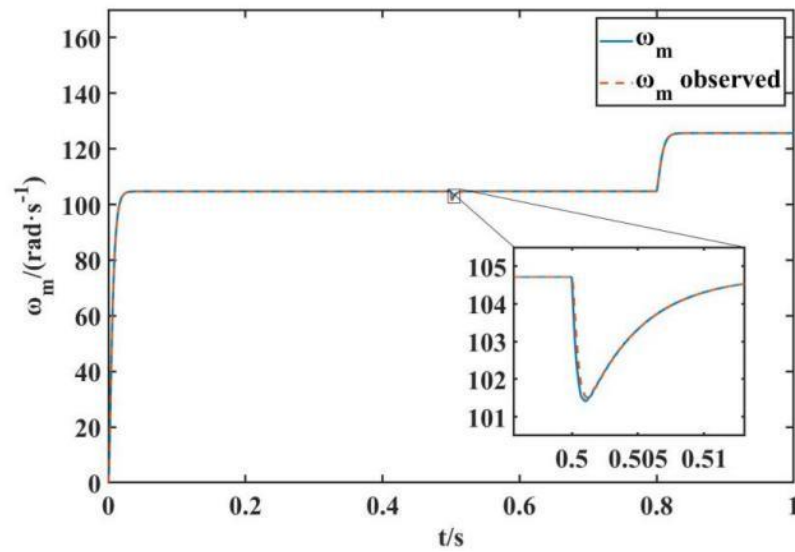


Figure 13. IGA-NRLSMC+ESO ω_m observed curve.

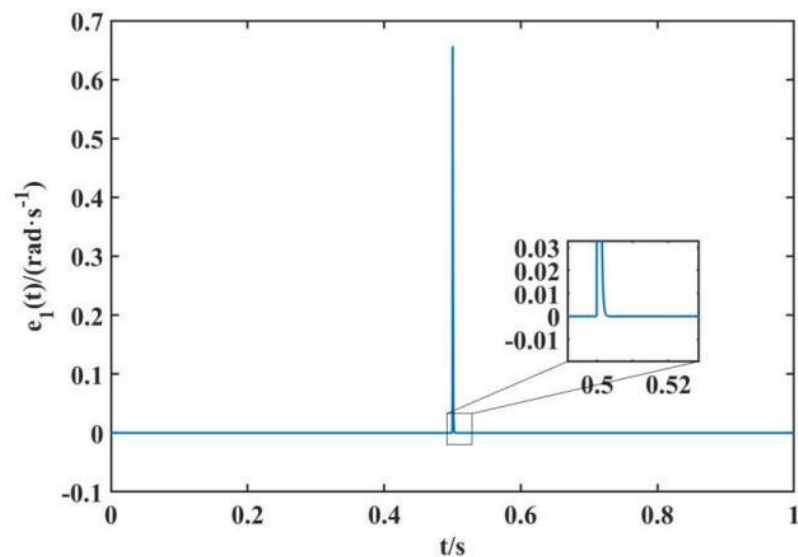


Figure 14. IGA-NRLSMC+ESO ω_m observed error curve.

The speed curves for the four-speed controllers are shown in Figure 9. According to the speed comparison presented in Table 5, the IGA-NRLSMC+ESO speed controller's curve exhibits no overshoot during startup and the shortest response time of 0.035 s. This response time is 0.125 s, 0.065 s, and 0.02 s faster than the response times of the other three controllers, respectively. When a load of 0.2 N·m is applied at 0.5 s, the IGA-NRLSMC+ESO controller demonstrates the shortest adjustment time of 0.02 s while maintaining the lowest decline. This adjustment time is 0.16 s, 0.06 s, and 0.01 s less than the adjustment times of the other three controllers, respectively. Even when the speed is increased to 1200 rpm at 0.8 s, the IGA-NRLSMC+ESO controller's curve remains free of overshoot and exhibits the shortest adjustment time of 0.035 s. This adjustment time is 0.085 s, 0.045 s, and 0.015 s less than the adjustment times of the other three controllers, respectively.

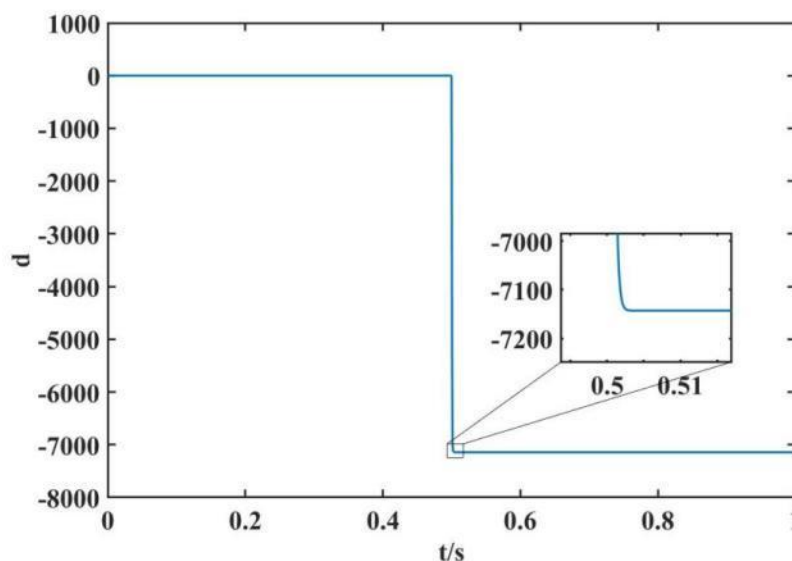


Figure 15. IGA-NRLSMC+ESO total disturbance observed curve.

Table 5. Speed comparison.

Speed Controller	Start		Apply Load		Increase Speed	
	Overshoot	Response time	Decline Volume	Adjustment Time	Overshoot	Adjustment Time
PID	12.9%	0.16 s	17.5%	0.18 s	2.1%	0.12 s
SMC	0%	0.1 s	11%	0.08 s	0%	0.08 s
NRLSMC+ESO	0%	0.055 s	3.4%	0.03 s	0%	0.05 s
IGA+NRLSMC+ESO	0%	0.035 s	3.2%	0.02 s	0%	0.035 s

Figure 10 illustrates the speed error curves for the four-speed controllers. Table 6 compares the speed error, demonstrating that all controllers exhibit speed errors of 1000 rpm and 200 rpm during startup and speed increase, respectively, due to the set speed being 1000 rpm and 1200 rpm. When the load is applied at 0.5 s, the IGA-NRLSMC+ESO speed controller displays the smallest speed error of 32 rpm, which is 143 rpm, 78 rpm, and 2 rpm less than the speed errors of the other three controllers.

Table 6. Speed error comparison.

Speed Controller	Start	Apply Load	Increase Speed
PID	1000 rpm	175 rpm	200 rpm
SMC	1000 rpm	110 rpm	200 rpm
NRLSMC+ESO	1000 rpm	34 rpm	200 rpm
IGA-NRLSMC+ESO	1000 rpm	32 rpm	200 rpm

Figures 11 and 12 display the three-phase current curves and torque curves, respectively, obtained for the four-speed controllers. The response time and adjustment time for the three-phase current and torque during startup, load application, and speed increase are equivalent to those of the speed. Table 7 compares the three-phase current and torque, indicating that the IGA-NRLSMC+ESO speed controller achieves steady-state values for the current and torque curves faster than the other three controllers during startup, load application, and speed increase.

Table 7. Comparison of three-phase current and torque.

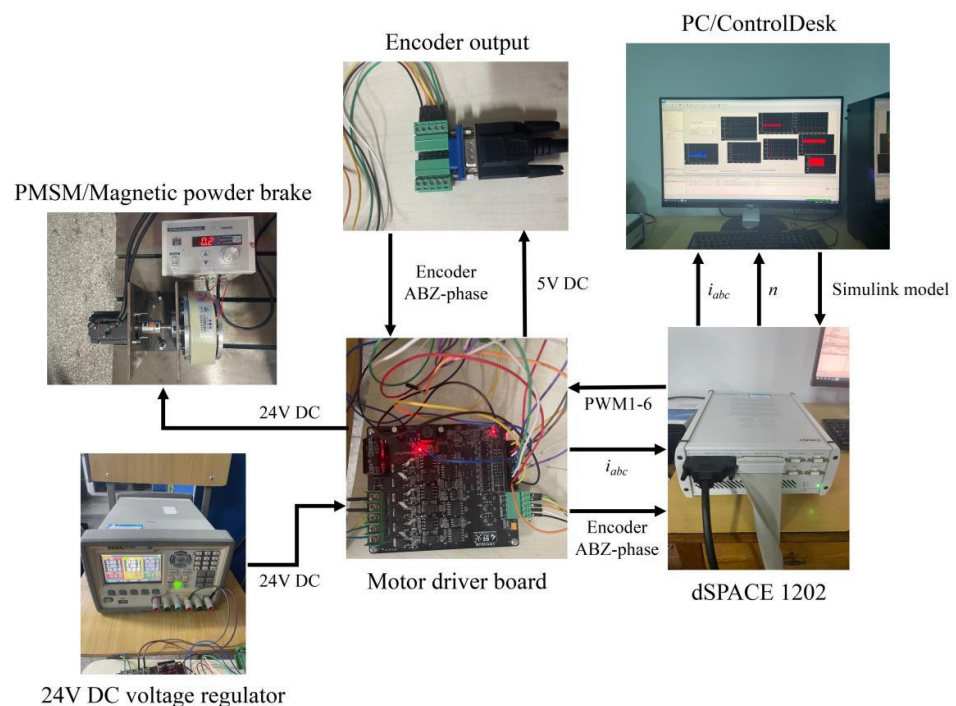
Speed Controller	Start Response Time	Apply Load Adjustment Time	Increase Speed Adjustment Time
PID	0.16 s	0.18 s	0.12 s
SMC	0.1 s	0.08 s	0.08 s
NRLSMC+ESO	0.055 s	0.03 s	0.05 s
IGA-NRLSMC+ESO	0.035 s	0.02 s	0.035 s

Figure 13 displays the observed ω_m curve for IGA-NRLSMC+ESO, which achieves fast tracking when the load is suddenly increased, exhibiting an observed error of 0.657 rad/s and a response time of 0.0035 s, as demonstrated in Figure 14. Furthermore, the IGA-NRLSMC+ESO total disturbance observed curve in Figure 15 demonstrates that the system can rapidly estimate changes in total disturbance, with a response time of 0.0035 s when the load changes at 0.5 s. Hence, by incorporating ESO, the control system's anti-interference capability is further improved.

Therefore, according to the simulation results of the four-speed controllers, it can be concluded that the PMSM control system with IGA-NRLSMC+ESO has the advantages of no overshoot, fast response, and strong robustness compared to PID, SMC, and NRLSMC+ESO.

7. Experimental Verification

To verify the performance of IGA-NRLSMC+ESO, an RCP experimental platform is established using dSPACE 1202, as depicted in Figure 16. The platform comprises a PC, dSPACE 1202, a motor driver board, a PMSM, a 1000-line optical encoder, and a 24V DC voltage regulator. The PMSM control system's RCP model is developed in MATLAB/Simulink and compiled into C code, which can be executed on the dSPACE 1202. The dSPACE 1202 is connected to the motor drive board and the optical encoder signal output interface, following the RTI module's interface in the RCP model. During motor operation, experimental data can be monitored in real-time through ControlDesk on the PC, allowing for online parameter adjustments.

**Figure 16.** RCP experimental platform of PMSM control system.

The motor parameters used in the experiment are shown in Table 2, and the controller parameters are set the same as the simulation. The experimental condition 1 is the speed step condition where the initial given speed is 1000 rpm and the speed increases to 1200 rpm after 3 s. The experimental results are shown in Figures 17–22.

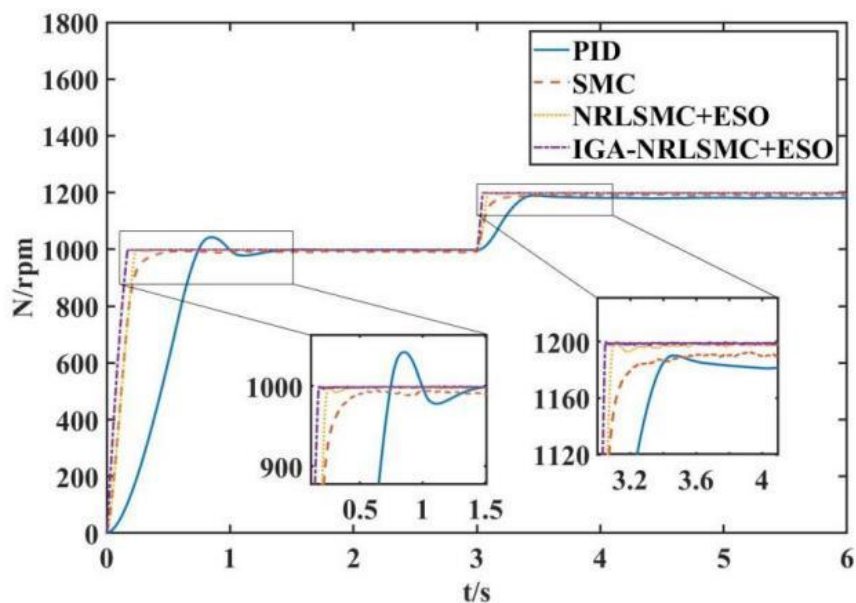


Figure 17. Experimental speed curve.

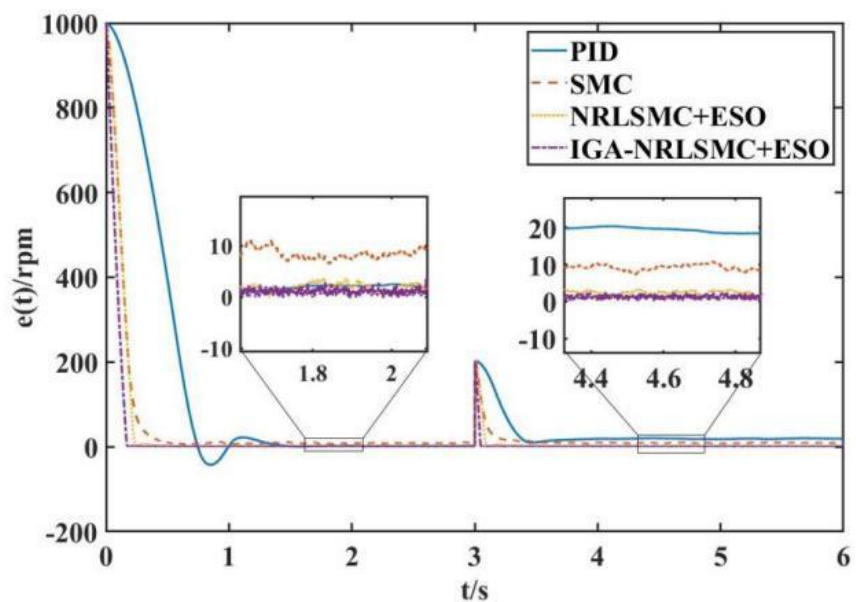


Figure 18. Experimental speed error curve.

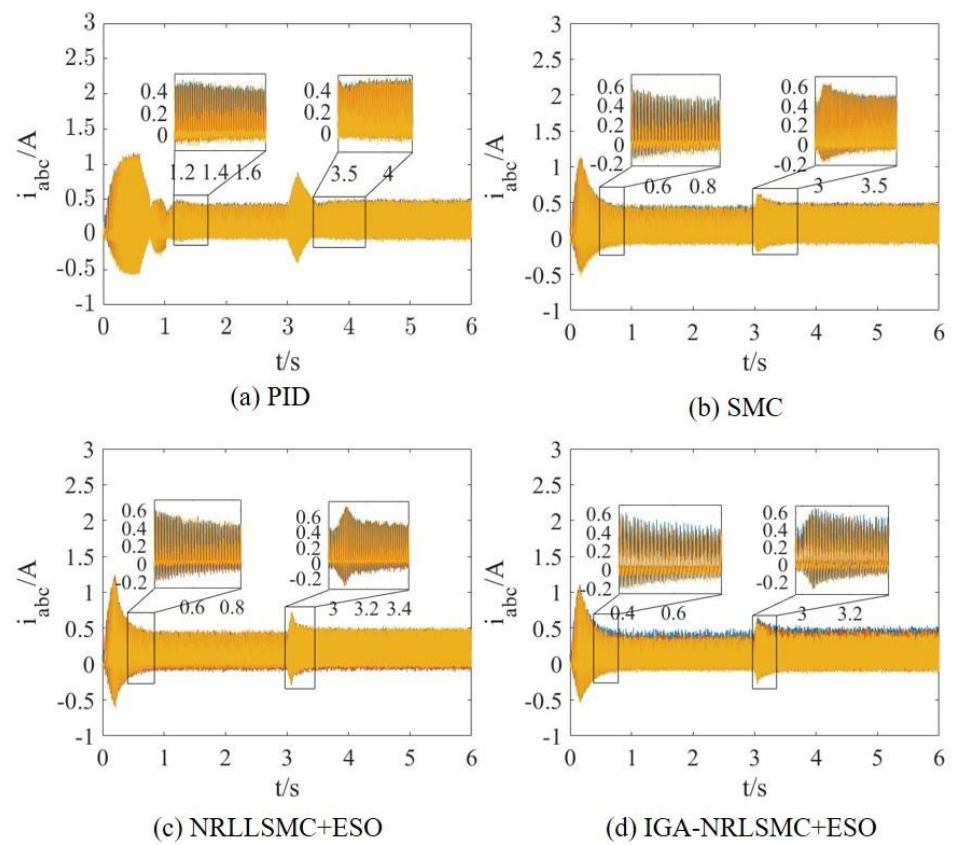


Figure 19. Experimental three-phase current curve.

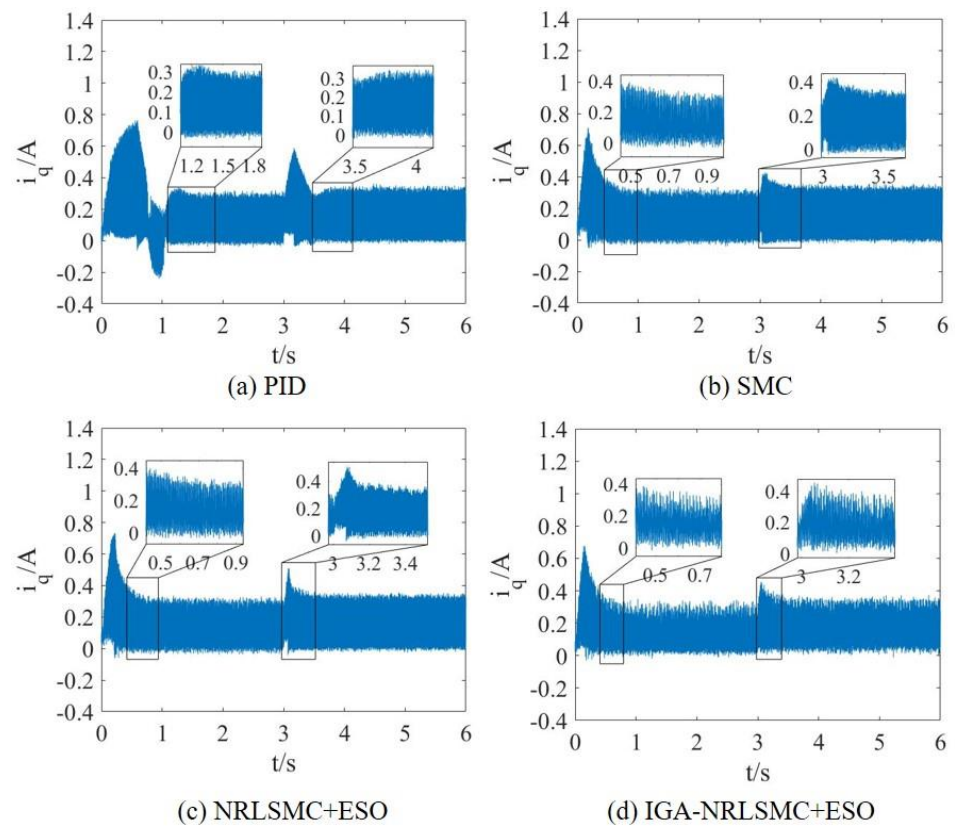


Figure 20. Experimental q -axis current curve.

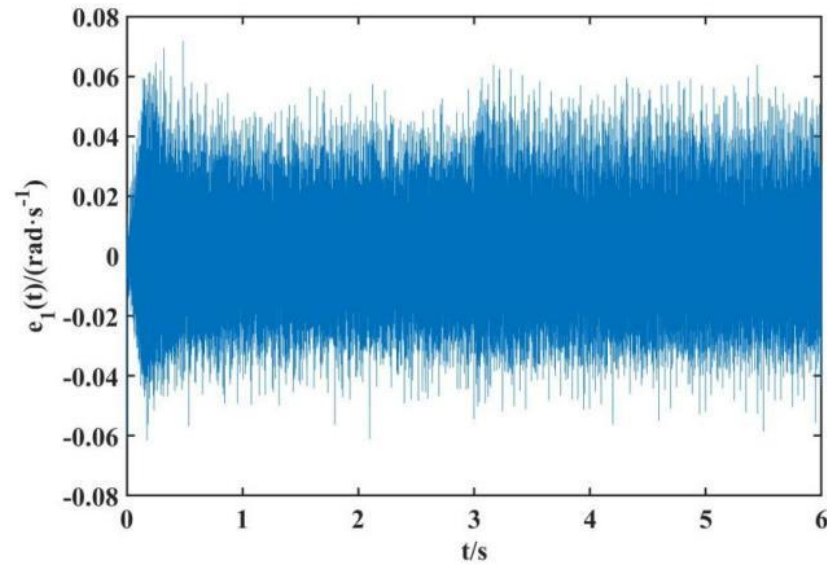


Figure 21. Experimental IGA-NRLSMC+ESO ω_m observed error curve.

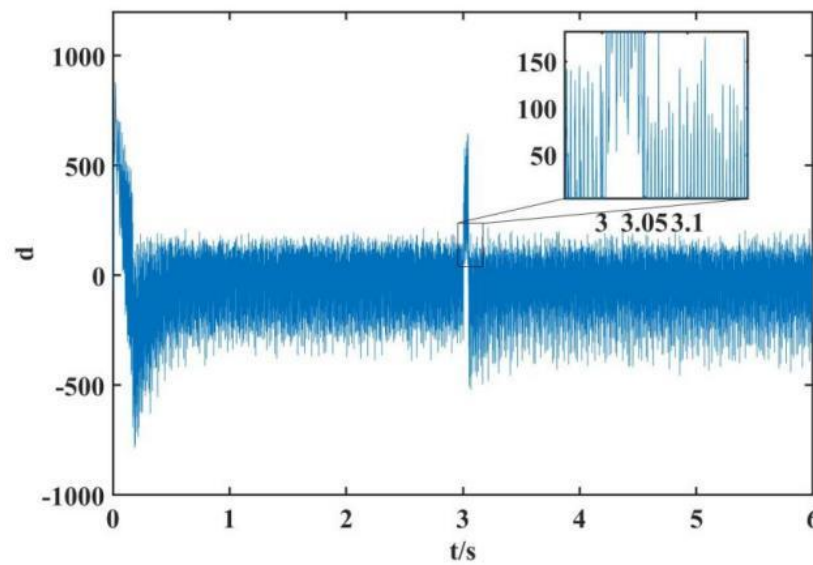


Figure 22. Experimental IGA-NRLSMC+ESO total disturbance observed curve.

The speed curves obtained from the experiments with four different speed controllers are shown in Figure 17. Based on the experimental speed comparison presented in Table 8, it can be observed that the speed curve obtained by IGA-NRLSMC+ESO has the shortest response time of 0.17 s, which is 1.41 s, 0.47 s, and 0.08 s less than the other three speed controllers, respectively, with no overshoot. Furthermore, when the speed steps to 1200 rpm after 3 s, there is still no overshoot, and the adjustment time is the shortest at 0.05 s, which is 0.98 s, 0.57 s, and 0.06 s less than the other three speed controllers, respectively. Therefore, IGA-NRLSMC+ESO has the advantages of no overshoot, fast response, and strong robustness compared to PID, SMC, and NRLSMC+ESO.

Table 8. Experimental speed comparison.

Speed Controller	Start		Increase Speed	
	Overshoot	Response Time	Overshoot	Adjustment Time
PID	4.3%	1.58 s	0.8%	1.03 s
SMC	0%	0.64 s	0%	0.62 s
NRLSMC+ESO	0%	0.25 s	0%	0.11 s
IGA-NRLSMC+ESO	0%	0.17 s	0%	0.05 s

The speed error curves obtained from experiments using four different speed controllers are presented in Figure 18. Based on the experimental speed error comparison given in Table 9, it can be observed that when the PMSM runs at a steady state of 1000 rpm, IGA-NRLSMC+ESO has the smallest steady-state error of 0–2.5 rpm. Similarly, when the speed is increased to 1200 rpm after 3 s, IGA-NRLSMC+ESO also maintains the smallest steady-state error of 0–2 rpm. These results demonstrate that IGA-NRLSMC+ESO offers strong robustness and outperforms PID, SMC, and NRLSMC+ESO regarding the steady-state error.

Table 9. Experimental speed error comparison.

Speed Controller	1000 rpm Steady State Error	1200 rpm Steady State Error
PID	1.5~2.5 rpm	18~20.5 rpm
SMC	7~12 rpm	7~11 rpm
NRLSMC+ESO	0~4 rpm	1~4 rpm
IGA-NRLSMC+ESO	0~2.5 rpm	0~2 rpm

The current curves of the three phases obtained from the experiments with four different speed controllers are presented in Figure 19. It can be observed that the three-phase currents obtained by IGA-NRLSMC+ESO reach the steady state value faster during both start-up and speed increase compared to the other three speed controllers. This observation is consistent with the simulation results.

The q -axis current curves obtained from the experiments with four different speed controllers are shown in Figure 20. It can be observed that the q -axis currents obtained by IGA-NRLSMC+ESO reach the steady state value first during the start-up and speed increase compared to the other three speed controllers. The response time of the q -axis current is the same as the experimental three-phase current. These results further demonstrate the strong robustness of IGA-NRLSMC+ESO, giving it an advantage over PID, SMC, and NRLSMC+ESO.

Figures 21 and 22 illustrate the experimental results of the IGA-NRLSMC+ESO control system, showing the observed error curve of ω_m and the total disturbance observed curve, respectively. As shown in Figure 21, the IGA-NRLSMC+ESO can accurately observe ω_m in practice, with a small observation error even when the speed is increased, and the observed error of ω_m is only between -0.06 and 0.06 rad/s throughout the process. Figure 22 indicates that IGA-NRLSMC+ESO can rapidly detect the change of the total disturbance, with a response time of 0.05 s when the speed changes after 3 s. These results further confirm that the introduction of ESO enhances the anti-disturbance capability of the control system.

The experimental results for the applied load condition with a sudden increase of 0.2 N·m load, while the motor runs steadily at 1000 rpm, are shown in Figure 23 under experimental condition 2.

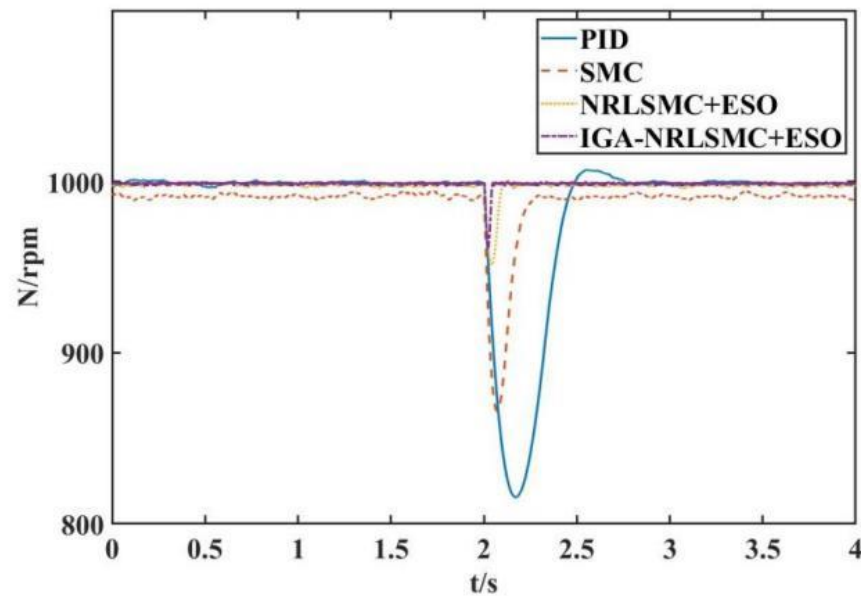


Figure 23. Experimental loading speed curve.

Figure 23 illustrates the loading speed curves obtained by four different speed controllers in the experiment, under condition 2 which is sudden loading with 0.2 N·m at 1000 rpm. As shown in Table 10, the speed curve obtained by IGA-NRLSMC+ESO exhibits the smallest drop of 43 rpm, which is 142 rpm, 91 rpm, and 7 rpm less than the other three speed controllers, respectively. Additionally, IGA-NRLSMC+ESO demonstrates the shortest adjustment time of 0.05 s, which is 0.77 s, 0.25 s, and 0.07 s less than the other three speed controllers. These results further confirm that IGA-NRLSMC+ESO enhances the system's robustness.

Table 10. Comparison of experimental loading speed.

Speed Controller	Decline Volume	Adjustment Time
PID	185 rpm	0.82 s
SMC	134 rpm	0.3 s
NRLSMC+ESO	50 rpm	0.12 s
IGA-NRLSMC+ESO	43 rpm	0.05 s

Comparing the experimental and simulation results under the same working conditions, the speed curve, speed error curve, three-phase current curve, q-axis current curve, and loading speed curve obtained by adopting IGA-NRLSMC+ESO in the experiment are superior to the other three speed controllers. This confirms that the system can benefit from the advantages of no overshoot, fast response, and strong robustness, consistent with the simulation results, thus verifying the accuracy of the simulation results.

5. Conclusions

A nonlinear reaching law sliding mode control method based on ESO and IGA is proposed in this paper, to solve the problems of slow reaching rate and jitter in the traditional sliding mode control and the difficulty of sliding mode parameters tuning effectively. The parameters of the above sliding mode controller are tuned by IGA. Simulation and experimental results show that the nonlinear reaching law has faster convergence speed and better vibration suppression effect compared with the traditional reaching law; in the controller parameters tuning, the IGA has faster iteration speed and better global search ability compared with the normal GA; and the PMSM control system with IGA-

NRLSMC+ESO has significant advantages over PID, SMC, and NRLSMC+ESO in terms of overshoot, response speed, and robustness, which effectively improves the control effect and anti-disturbance capability of PMSM. The proposed IGA-NRLSMC+ESO method has the advantages of strong anti-disturbance capability, small jitter, and self-adjusting parameters, which solves the problem of the inherent jitter of the sliding mode and the difficulty of the sliding mode self-adjusting parameters.

Author Contributions: Conceptualization, S.L. and H.L.; methodology, H.W. and C.Y.; validation, S.L., H.L. and H.W.; formal analysis, J.G.; resources, H.W.; project administration, R.F.; writing—original draft preparation, S.L. and H.L.; writing—review and editing, S.L., H.W. and C.Y. All authors have read and agreed to the published version of the manuscript.

Funding: This research was funded by “The overseas study visit and training program for outstanding young backbone talents of Anhui Province, grant number gxgwx2021035”, “The innovation team of Anhui Polytechnic University”, “Graduate Student Innovation Project of Anhui Province, grant number 2022xscx097”, “Anhui Polytechnic University-Jiujiang District Industrial Collaborative Innovation Special Fund Project, grant number 2022cyxtb4”, and the Enterprise Cooperation Project of Anhui Future Technology Research Institute.

Data Availability Statement: The data are not publicly available due to privacy and ethical restrictions.

Conflicts of Interest: The authors declare no conflict of interest.

References

- Deng, W.; Yao, J. Extended-state-observer-based adaptive control of electrohydraulic servomechanisms without velocity measurement. *IEEE/ASME Trans. Mechatron.* **2019**, *25*, 1151–1161.
- Deng, W.; Zhou, H.; Zhou, J.; Yao, J. Neural network-based adaptive asymptotic prescribed performance tracking control of hydraulic manipulators. *IEEE Trans. Syst. Man Cybern. Syst.* **2022**, *53*, 285–295.
- Zyadat, Z.; Horri, N.; Innocente, M.; Statheros, T. Observer-Based Optimal Control of a Quadplane with Active Wind Disturbance and Actuator Fault Rejection. *Sensors* **2023**, *23*, 1954.
- Deng, W.; Yao, J.; Wang, Y.; Yang, X.; Chen, J. Output feedback backstepping control of hydraulic actuators with valve dynamics compensation. *Mech. Syst. Signal Process.* **2021**, *158*, 107769.
- Wang, C.; Zhu, Z. Fuzzy Logic Speed Controller with Adaptive Voltage Feedback Controller of Permanent Magnet Synchronous Machine. In Proceedings of the 2018 XIII International Conference on Electrical Machines (ICEM), Alexandroupoli, Greece, 3–6 September 2018; pp. 1524–1530.
- Mesloub, H.; Benchouia, M.T.; Boumaaraf, R.; Goléa, A.; Goléa, N.; Becherif, M. Design and implementation of DTC based on AFLC and PSO of a PMSM. *Math. Comput. Simul.* **2020**, *167*, 340–355.
- Ali, N.; Ur, R.A.; Alam, W.; Maqsood, H. Disturbance observer based robust sliding mode control of permanent magnet synchronous motor. *J. Electr. Eng. Technol.* **2019**, *14*, 2531–2538.
- Miao, Z.C.; Zhang, W.B.; Yu, X.F.; Huang, X. Fractional Order Integral Sliding Mode Control For Pmsm Based On Speed Estimation. *Acta Energ. Sol. Sin.* **2021**, *42*, 28–34.
- Saeed, S.; Zhao, W.; Wang, H.; Tao, T.; Khan, F. Fault-tolerant deadbeat model predictive current control for a five-phase PMSM with improved SVPWM. *Chin. J. Electr. Eng.* **2021**, *7*, 111–123.
- Li, Y.; Sun, R.; Xia, Y.; Gu, C. A Sliding Mode Control Method with Improved Rapid Power Approximation Law. *J. Xi'an Jiaotong Univ.* **2022**, *56*, 118–126.
- Chuang, C.; Bo, W.; Yong, Y.; Zhi, H.; Dian, X. An Improved Exponential Reaching Law Based-Sliding Mode Observer for Speed-Sensorless Induction Motor Drive. *Trans. China Electrotech. Soc.* **2020**, *35*, 155–163.
- Kang, E.L.; He, J.Z.; Wang, Y.C. Design of non-singular fast terminal sliding mode controller for permanent magnet synchronous motors. *Electr. Mach. Control* **2021**, *25*, 58–64.
- Qu, L.Z.; Qiao, W.; Qu, L.Y. An extended-state-observer-based sliding-mode speed control for permanent-magnet synchronous motors. *IEEE J. Emerg. Sel. Top. Power Electron.* **2020**, *9*, 1605–1613.
- Lu, E.; Li, W.; Yang, X.; Liu, Y. Anti-disturbance speed control of low-speed high-torque PMSM based on second-order non-singular terminal sliding mode load observer. *ISA Trans.* **2019**, *88*, 142–152.
- Zhang, R.Y.; Zheng, C.S.; Shi, P.C.; Zhao, L.F.; Gong, C.F.; Zhou, C.L. Sensorless control of PMSM based on improved PSO and generalized fifth order CKF algorithm. *Electr. Mach. Control* **2021**, *25*, 120–128.
- Yan, J.Z.; Zhuan, X.T. Parameter self-tuning and optimization algorithm based on reinforcement learning. *CAAI Trans. Intell. Syst.* **2022**, *17*, 341–347.
- Lizhou, L.; Youwei, W. Double drive fruit fly optimization algorithm and its application in PID controller. *Control Decis.* **2021**, *36*, 2225–2233.

18. Xiao, L.Q. Parameter tuning of PID controller for beer filling machine liquid level control based on improved genetic algorithm. *Comput. Intell. Neurosci.* **2021**, *2021*, 7287796.
19. Tran, H.K.; Son, H.H.; Duc, P.V.; Trang, T.T.; Nguyen, H.-N. Improved genetic algorithm tuning controller design for autonomous hovercraft. *Processes* **2020**, *8*, 66.
20. Cao, F.L. PID controller optimized by genetic algorithm for direct-drive servo system. *Neural Comput. Appl.* **2020**, *32*, 23–30.
21. Li, S.; Zhao, C.; Su, X.; Wang, X. Temperature and humidity control for environmental test chamber based on genetic algorithm optimized parameters of PID controller. *J. Nanjing Univ. Sci. Technol.* **2017**, *41*, 511–518.
22. Pilla, R.; Gorripotu, T.S.; Karlapudy, A.M. Design and implementation of a nonlinear controller and observer for inverter fed permanent magnet synchronous motor drive using dSPACE DS1103 controller board. *Int. J. Autom. Control* **2021**, *15*, 78–98.
23. Chen, Y.; Li, M.; Gao, Y.W.; Chen, Z.Y. A sliding mode speed and position observer for a surface-mounted PMSM. *ISA Trans.* **2019**, *87*, 17–27.
24. Gao, Y.; Liu, W.G.; Luo, G.Z. New dual-sliding mode control method of PMSM based on dSPACE. *J. Cent. South Univ.* **2015**, *46*, 2036–2043.
25. Liu, J.K. *MATLAB Simulation for Sliding Mode Control*; Tsinghua University Press: Beijing, China, 2005.
26. Wang, Y.; Feng, Y.; Zhang, X.; Liang, J. Zhang. A new reaching law for antidisturbance sliding-mode control of PMSM speed regulation system. *IEEE Trans. Power Electron.* **2019**, *35*, 4117–4126.
27. Li, J.; Qi, X.H.; Xia, Y.Q.; Gao, Z.Q. On Linear/Nonlinear Active Disturbance Rejection Switching Control. *Acta Autom. Sin.* **2016**, *42*, 202–212.

Disclaimer/Publisher’s Note: The statements, opinions and data contained in all publications are solely those of the individual author(s) and contributor(s) and not of MDPI and/or the editor(s). MDPI and/or the editor(s) disclaim responsibility for any injury to people or property resulting from any ideas, methods, instructions or products referred to in the content.